Reconstructing magnetic fields of spiral galaxies from radiopolarimetric observations

Shneider, C.

Citation

Shneider, C. (2015, December 17). *Reconstructing magnetic fields of spiral galaxies from radiopolarimetric observations*. *PhD Thesis*. Retrieved from https://hdl.handle.net/1887/37053

5

A 3D magnetic field model for NGC 6946

C. Shneider, M. Haverkorn, A. Williams, G. Heald

Astronomy & Astrophysics, 2015
To be submitted

Abstract

Context. Spiral galaxies generally host regular, large-scale magnetic fields in their disks, following spiral arms. For highly inclined galaxies, large-scale vertical magnetic field components are also usually observed above and below the disk, in the gaseous halo. These magnetic field lines in halos are generally observed to have an X-shape. This could indicate a helical magnetic field structure, naturally produced by a combination of poloidal and toroidal magnetic fields.
Aims. We would like to determine whether an X-shape magnetic field structure in the almost face-on galaxy NGC 6946 can explain observations of the degree of linear polarization (p) in this galaxy, at various wavelengths.
Methods. We construct a 3D divergence-free magnetic field model. The model contains axisymmetric spiral magnetic fields in the galaxy disk, and helical fields in the halo, which are symmetric about the mid-plane. Using suitable thermal electron and cosmic ray electron distributions, we simulate synchrotron emission from this galaxy. We use p as a diagnostic, and compare our findings to polarimetric observations at wavelengths from five radio

bands between 3.5 cm and 23 cm. We assume that wavelength-dependent depolarization is negligible at our shortest wavelength, and use the observations at this wavelength to determine the amount of wavelength-independent depolarization. The other wavelengths are then scaled by this amount. We simulate p maps for varying regular magnetic field strengths and use the reduced chi-square statistic to determine the best-fit regular field strength for the whole galaxy.

Results. An X-shape field is a feasible model for the 3D regular magnetic field configuration of NGC 6946. Our best-fit field model yields a $\sim 10\,\mu$G field strength in good agreement with earlier estimates that used radio synchrotron observations and equipartition arguments. The model approximately reproduces the azimuthal variation in polarized intensity in the inner galaxy, but still overproduces polarization at certain azimuths, possibly due to lack of turbulent fields in the models.

5.1 Introduction

Magnetic fields are important dynamical constituents of galaxies. They thread the interstellar medium (ISM) and influence virtually all interstellar matter, except for the densest interiors of molecular clouds, via the Lorentz force. Ion-neutral collisions ensure that even cold atomic clouds, with an ionization degree of $10^{-4} - 10^{-3}$, remain tightly coupled to charged particles and, consequently, to the magnetic field (Ferrière 2001). Moreover, magnetic fields affect the thermal conductivity of the ISM (Orlando et al. 2008), the propagation of cosmic rays (Strong et al. 2007; Yan 2015), and the dynamics of molecular clouds and star formation (Hennebelle & Falgarone 2012). Essentially, the magnetic field lines are mostly 'frozen-in' into the interstellar gas. As a consequence, their field geometry is subject to distortion by plasma flows such as from supernova remnants, H II regions, jets, and stars. Additionally, their field strength is varied - amplified, for example, by the combination of large-scale differential rotation and small-scale turbulent motions in galactic disks, as in the Milky Way (Steenbeck & Krause 1966; Parker 1971; Vainshtein & Ruzmaikin 1971), and locally diminished by magnetic reconnection. Turbulent motions are also responsible for the dramatic decrease in the (large-scale) magnetic field diffusion time (Parker 1979). Besides being present in the disks of galaxies, significant magnetic fields are also present in (gaseous) galactic halos where they provide pressure support against the gravity of the halo gas and, thereby, contribute to the hydrostatic balance of the ISM (Boulares & Cox 1990). They also play a role in the disk-halo interaction by transporting magnetic flux from the disk to the halo (Hanasz et al. 2009b), influencing superbubble break-out (Ferrière 2001; Heesen et al. 2009), and transferring charged particles from the galaxy into the intergalactic medium.

Diffuse synchrotron emission traces magnetic fields in galaxies yielding information on the integrated magnetic component perpendicular to the line-of-sight. Traditionally, galactic magnetic fields are divided into small-scale and large-scale fields (see for example Haverkorn (2014)). The term 'large-scale' fields (also called mean, average, global, regular, uniform or coherent) indicates the component of the magnetic field that is coherent on length scales of the order of a galaxy. ‘Small-scale’ fields (also called random, tangled, or turbulent) describe the magnetic field component at the scale of ISM turbulence. A large-scale spiral field structure along the disk plane that is aligned with the optical or gaseous spiral arms is observed in nearby spiral galaxies (Krause 2014). Synchrotron emission from halos is more straightforward to study in edge-on galaxies than in face-on galaxies since emission from the disk and halo is not superimposed. From linear polarization studies of edge-on galaxies (e.g., Dahlem et al. (1997); Tüllmann et al. (2000); Krause (2009); Hanasz et al. (2009b); Heesen et al. (2009); Soida et al. (2011); Mora & Krause (2013)) we learned that many halos possess vertical magnetic field components, with field orientation fanning out from the center, forming an X-shape. Following the terminology used by other authors (Ferrière & Terral 2014, and refs. therein), we refer to such fields as ‘X-shape’. Whether the X-shaped field is observationally attributable to either the regular field or to the anisotropic turbulent field (ordered field with randomly varying direction on small scales) remains open. Based on polarization data from the WSRT-SINGS (Braun et al. 2007) (Westerbork Synthesis Radio Telescope - Spitzer Infrared Nearby Galaxies Survey) (Kennicutt et al. 2003, SINGS) galaxy sample, Braun et al. (2010) modeled quadrupolar fields that can be interpreted as X-shape fields. An X-shape field is thought to be common in galaxies and its inclusion in the magnetic field models of the Milky Way by Jansson & Farrar (2012a,b) improved overall fits to the rotation measure (*RM*) data. Horizontal and vertical components of the regular magnetic field in the disks and halos of spiral galaxies have been included in earlier models (e.g., see Berkhuijsen et al. (1997); Fletcher et al. (2011) for the case of M51).

X-shaped magnetic fields may be caused by various physical processes. When the X-shape arises from a large-scale magnetic field it is most likely due to a galactic wind which transports the disk field into the halo where the galactic wind occurs in conjunction with dynamo action (Brandenburg et al. 1993; Hanasz et al. 2009a,b; Moss et al. 2010; Hanasz et al. 2013; Gressel et al. 2013). Magnetohydrodynamical (MHD) simulations also show that an X-shape field naturally develops from dynamo action (e.g., Kulpa-Dybeł et al. (2011)). However, simulations incorporating all relevant physics such as turbulence, cosmic rays, supernovae, superbubbles, and the multi-phase nature of the ISM are still to be performed (Gressel et al. 2013). As the magnetic field is coupled to the gas, these X-shape fields may be related to the bi-conical gas outflows in hydrodynamical (HD) simulations (e.g., Dalla Vecchia & Schaye (2008, 2012)).

In this chapter, we study a magnetic field with a vertical magnetic field component in a face-on galaxy. We construct a simple magnetic field model that describes the disk and halo fields of a spiral galaxy and compare with radio polarimetric observations. The aim is to test whether the observed synchrotron (de)polarization can be explained by an X-shaped field in the halo. We choose the grand-design, spiral galaxy NGC 6946 for several reasons: its proximity of 5.5 Mpc (Kennicutt et al. 2003) implies access to high-quality observations, it has one of the highest star-formation rates among spiral galaxies (Beck 2007) which may imply high star formation driven outflows that would contribute to an X-shape, a companion galaxy whose interaction could distort the X-shape is absent, and earlier observations by Beck (2007) and Braun et al. (2010) suggest the presence of a

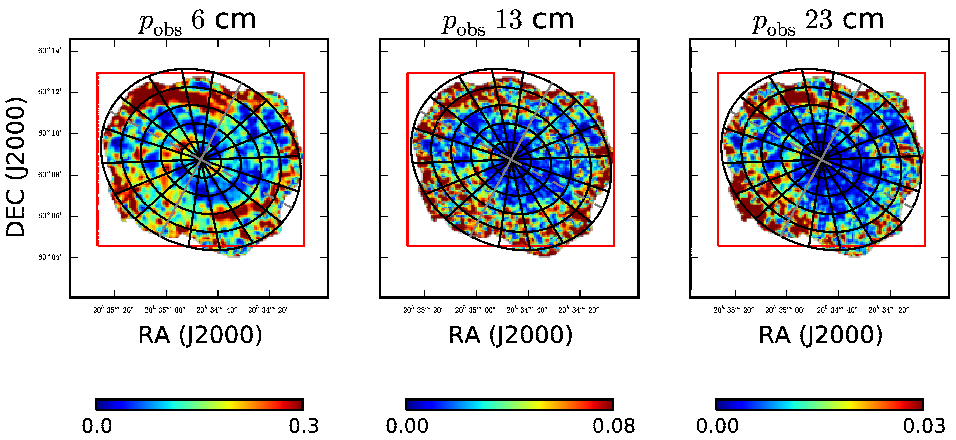

Figure 5.1: The observed degree of polarization p_{obs} maps are shown at 6 cm (left), 13 cm (center), and 23 cm (right). The red rectangle represents the size of the simulation box. The elliptical grid represents the partitioning of the galaxy into bins. The solid and dashed gray lines denote the minor and major axes, respectively, with the kinematically receding side of the galaxy towards the West.

vertical field.

This chapter is organized as follows: In Section 5.2 we present the data. In sections 5.3 and 5.4 we provide a description of the model. Results are presented in section 5.5 and discussed in section 5.6. Finally, we conclude and propose directions for future work in sections 5.7 and 5.8.

5.2 Observational data

We use continuum polarized and total synchrotron intensity observations of NGC 6946 (Williams & Heald 2015). These observations combine data from the Karl G. Jansky Very Large Array (VLA) and Effelsberg 100-m telescope at $\lambda\lambda\,3.5, 6$ cm by Beck (2007), WSRT at $\lambda\,13$ cm by Heald (2014), and the WSRT-SINGS survey at $\lambda\,23$ cm by Braun et al. (2010). The $\lambda\lambda\lambda\,13, 18$ and 23 cm data each have a $\sim$ 10 MHz bandwidth, consisting of 14, 11, and 15 channels, respectively, while the $\lambda\lambda\,3.5, 6$ cm are single channels, for a total of 42 maps. The WSRT data miss short spacing information. The largest detectable scales are $12.4'$ at 13 cm, and $22'$ at 23 cm. At the adopted distance to NGC 6946, the diameter of NGC 6946 is about $10'$ along the major axis. There is thus no missing large-scale structure at 13, 23 cm since the largest angular scales probed correspond to distances much larger than NGC 6946.

The thermal radio emission at $\lambda\,6$ cm is determined and subtracted using an an H-alpha image by Ferguson et al. (1999) and the method described in Heesen et al. (2014, Section 3.2). This final total intensity map is then used to generate non-thermal emission maps at all other available frequencies by assuming two separate synchrotron spectral index values of −0.7 and −1. These values of spectral index are representative of the spiral arms and interarm regions, respectively (Beck 2007; Tabatabaei et al. 2013).

Multichannel Stokes Q and U observations are first smoothed to a common 15″ beam resolution and then combined to arrive at polarized intensity (P) maps. In linear scale, 15″ corresponds to 400 pc. Subsequently, maps of observed degree of polarization ($p_{\rm obs}$) are obtained by taking P/I. A sample of three such maps is shown in Fig. 5.1 at $\lambda\lambda\lambda\, 6, 13$ and 23 cm. The color scale is adjusted at each wavelength in Fig. 5.1 to bring out small scale features.

5.3 Model

5.3.1 Magnetic field

We model the magnetic field in NGC 6946 using a large-scale field. This approach is useful to expand the Braun et al. (2010) analysis to a more physically motivated magnetic field model. We would like to explore the effect of large scale field structures on the observables when varying the parameters of a realistic large-scale field configuration. We adopt an X-shape field as defined in model 'Dd' of Ferrière & Terral (2014, see their Fig. 3). This model is selected because it reproduces the observationally recognizable polarized synchrotron radiation pattern observed in the halos of edge-on galaxies. The model is composed of an axisymmetric (ASS) spiral field in the disk and an X-shape field in the halo. Our X-shape regular magnetic field is physical in that it is divergence-free. Also, we choose to avoid a pure dipole and/or quadrupole magnetic field geometry as modeled in Braun et al. (2010) for qualitative comparison of field configurations. Quantitatively, dipole or quadrupole fields are not realistic as there are cross-field electric currents flowing in the interstellar plasma enclosed by the galaxy. In galactocentric cylindrical coordinates (r, ϕ, z) the field is given by

$$\begin{aligned} B_r &= -\frac{1}{3}\,\frac{r_1^3}{r^2\,z}\left[\sqrt{\left(\frac{z_1}{z}\right)} - \frac{z}{z_1}\right] B_z(r_1, z_1), \\ B_\phi &= \cot\left\{p_\infty + (p_0 - p_\infty)\left[1 + \left(\frac{|z|}{H_{\rm p}}\right)^2\right]^{-1}\right\} B_r, \\ B_z &= \frac{r_1^2}{r^2}\,B_z(r_1, z_1), \end{aligned} \tag{5.1}$$

with the reference field

$$B_z(r_1, z_1) = B_1\,\mathrm{sign}\,z_1\,\exp\left(-\frac{r_1}{L_{\rm B}}\right), \tag{5.2}$$

and with

$$r_1 = \frac{3}{2}\,r\left[\sqrt{\left(\frac{z_1}{z}\right)} + \frac{1}{2}\,\frac{z}{z_1}\right]^{-1},$$

where, in the above relations, r_1 is the radius of field lines at the reference height $z_1 = |z_1| \operatorname{sign} z$ and where sign z ensures that the model is symmetric since z/z_1 is always positive. Since field lines bend away and do not cross the mid-plane, in order to avoid having a singularity at $r = 0$ while keeping the field divergence-free, two values of z_1 with a positive/negative value for field lines above/below the mid-plane have to be taken. The physical meaning of the various model parameters in Eqs. (5.1) and (5.2) is as follows: p_0 is the pitch angle of the magnetic field line at the mid-plane ($m = 0$ mode), p_∞ is the pitch angle of the magnetic field line at an infinite height above/below the plane, H_p is the height above the disk plane corresponding to the average value of the pitch angle between mid-plane and infinity, B_1 is the peak value of the reference field, and L_B is the exponential scale length of the reference field.

The pitch angle of the counter-clockwise directed ‘magnetic spiral arms’ has a positive sign and is given by $p_0 = +28°$ which agrees well with the pitch angle of the optical spiral arms (Kennicutt 1981). Qualitatively, it may be expected that field lines become less tightly wound and thus have a larger pitch angle at higher latitudes since galactic differential rotation probably decreases with distance from the mid-plane (Ferrière & Terral 2014). Assuming that the magnetic spirals unwind at large vertical heights, $p_\infty = +90°$.

The overall field morphology is affected by the parameters z_1, H_p and L_B. The parameter z_1 affects the degree to which the ASS disk field is extended by a quadrupolar morphology in the halo. Large values of H_p preserve the initial pitch angle at the mid-plane up to large vertical heights while too small values make the spirals unwind at small distances from the mid-plane. Moreover, the value of L_B regulates the spread of field lines with a value of $1 < L_\mathrm{B} < 5$ kpc keeping the field lines from becoming too congested in the center at low L_B values.

In the frame of the galaxy, but now in Cartesian coordinates, the total field is

$$B_x = B_r \cos(\phi) - B_\phi \sin(\phi), \tag{5.3}$$

$$B_y = B_r \sin(\phi) + B_\phi \cos(\phi), \tag{5.4}$$

$$B_z = B_z. \tag{5.5}$$

The position angle of the major axis is 242° (Boomsma et al. 2008). Choosing the origin of the coordinate system to coincide with the dynamical center of the galaxy, with the x- and y- axes labeling the major and minor axes, respectively, the receding side of the galaxy is then labeled by $\phi = 0°$ and the approaching side by $\phi = 180°$. The observer’s frame (sky-plane) components are obtained for the inclination angle, l, of the galaxy from Eqs. (5.3)-(5.5) as (Braun et al. 2010)

$$B_{x'} = B_x, \tag{5.6}$$

$$B_{y'} = B_y \cos(l) - B_z \sin(l), \tag{5.7}$$

$$B_{\|} = B_y \sin(l) + B_z \cos(l), \tag{5.8}$$

where $(x', y', \|)$ are the major axis, minor axis, and line of sight, respectively. The inclination angle is taken as $l = 33°$ (Heald et al. 2009).

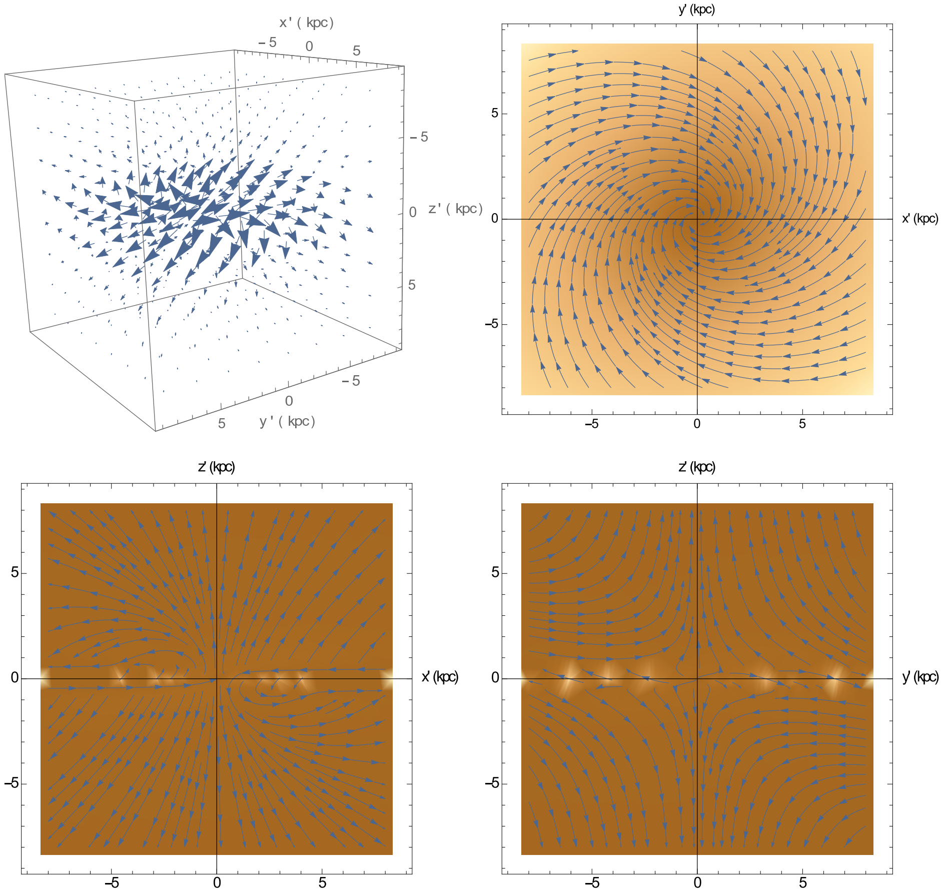

Figure 5.2: The regular magnetic field is shown using standard model parameters (see Section 5.4) viewed almost edge-on from an arbitrary angle. Top left: the 3D regular magnetic field vectors as simulated in a $16 \times 16 \times 16\,\mathrm{kpc}^3$ volume. The other panels show magnetic field components in slices through this cube in orthogonal directions. The direction of the slices are shown in the axes, and the slices are taken close to midway through the cube. The blue lines show the magnetic field direction in the plane of the slice, and the color scale shows the strength of the field component in that slice.

5.3.2 Densities

We focus on the diffuse ionized emission as this is more significant than H ii regions for Faraday rotation, owing to its larger filling factor (Beck & Wielebinski 2013). Although both the warm ionized medium (WIM) component and the hot ionized medium (HIM) contribute to the thermal electron density (n_e), the HIM component has a negligible affect on depolarization. This is on account of the HIM being so dilute with $n_e \sim 10^{-3}$ cm^{-3}

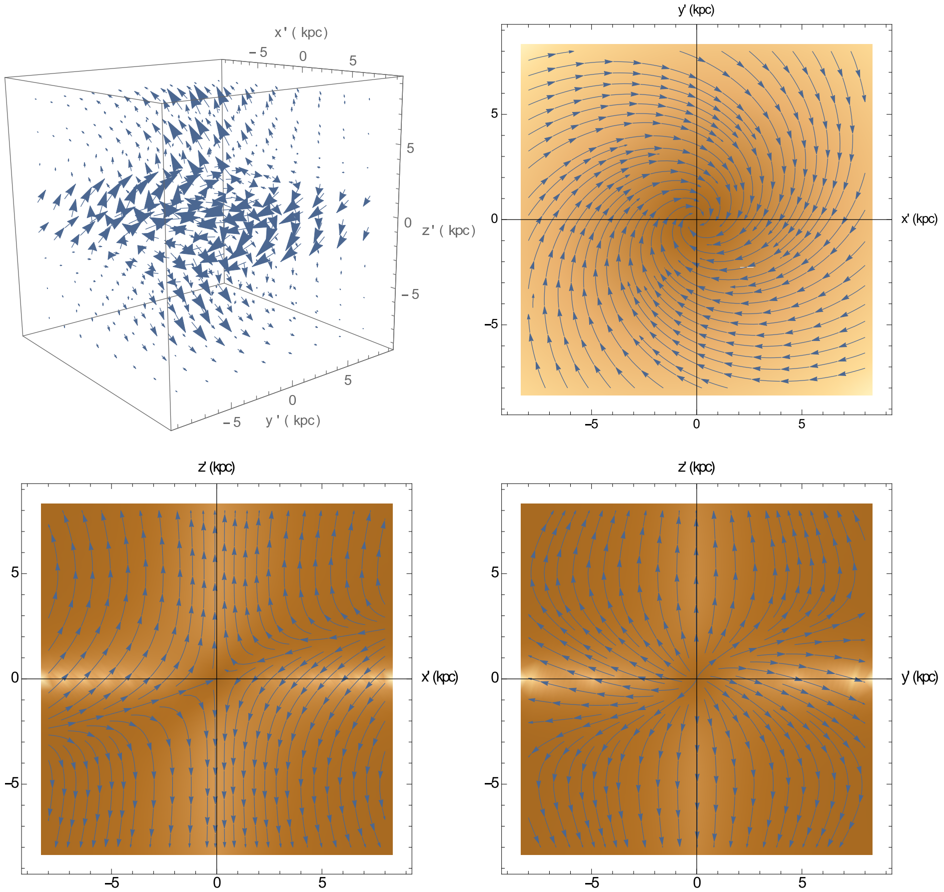

Figure 5.3: As in Fig. 5.2 but using best-fit model parameters (see Section 5.5).

(Haverkorn & Spangler 2013, Table 1).

In our model, cosmic rays are assumed to distribute homogeneously. Consequently, the synchrotron emissivity ε scales with the magnetic field as

$$\varepsilon\,(\mathbf{x}') = c\,\left(B_{x'}^2 + B_{y'}^2\right)(\mathbf{x}')\,, \tag{5.9}$$

with c a constant proportional to the cosmic ray electron density. This assumed quadratic dependence of emissivity on magnetic field is an observationally consistent scaling for disks and halos of galaxies (Sokoloff et al. 1998, 1999).

5.3.3 Stokes parameters

The degree of polarization p is the ratio of polarized intensity (P) to total intensity (I) and is given by

$$p = \frac{P}{I} \tag{5.10}$$

with $0 \leq p \leq p_0$ where $p_0 = 0.75$ is chosen as the maximum intrinsic degree of polarization. A synchrotron spectral index between -0.5 to -1.1 corresponds to an intrinsic polarization value of $70 - 76\%$. Since we are using -0.7, p_0 should in principle be closer to 70%. However, from the large errors both in the observations in the outermost pair of rings at all frequencies and from all observations at low frequencies, a p_0 of 0.75 is fine.

The Stokes parameters composing the polarized intensity and total intensity in Eq. (5.10) are given by

$$\begin{aligned}
I &= \int_0^{L_{\text{tot}}} \varepsilon\left(\boldsymbol{x}'\right)\, dz, \\
Q &= \int_0^{L_{\text{tot}}} \varepsilon\left(\boldsymbol{x}'\right) \cos\left[2\left(\psi_0 + 0.81\,\lambda^2 \int_{z'}^{L_{\text{tot}}} n_{\text{e}}\, B_{\|}\left(\boldsymbol{x}'\right) dz''\right)\right] dz', \\
U &= \int_0^{L_{\text{tot}}} \varepsilon\left(\boldsymbol{x}'\right) \sin\left[2\left(\psi_0 + 0.81\,\lambda^2 \int_{z'}^{L_{\text{tot}}} n_{\text{e}}\, B_{\|}\left(\boldsymbol{x}'\right) dz''\right)\right] dz', \\
P &= \sqrt{Q^2 + U^2},
\end{aligned}$$

with magnetic field defined in Eqs. (5.6) - (5.8), the emissivity in Eq. (5.9), and intrinsic polarization angle (Berkhuijsen et al. 1997, and Eq. (3.4) of Chap. 3)

$$\psi_0 = \tfrac{1}{2}\pi - \arctan\left[\cos(l)\tan(\phi)\right] + \arctan\left(B_{y'}/B_{x'}\right).$$

Magnetic field strengths are in μG, λ is the observing wavelength (m), dz'' and dz' are increments along the line of sight with positive direction pointing toward the observer, $L_{\text{tot}} = 2\,L_d + 2\,L_h$ is the total path length (pc) with L_d and L_h the assumed scale heights of the thermal disk and thermal halo, respectively, and z' denotes the location of each emitting source along the line of sight with $z' = 0$ marking the location of the farthest source from the observer. In the model described above, the regular magnetic field strength and electron density vary along a line of sight. This causes wavelength-independent depolarization due to varying intrinsic polarization angles along the line of sight, and wavelength-dependent depolarization due to Faraday rotation (differential Faraday rotation). However, because turbulent fields are not modeled, wavelength-dependent depolarization due to internal Faraday dispersion is not described.

5.3.4 Simulated Volume

We simulate a representative galactic volume of $16 \times 16 \times 16\,\text{kpc}^3$ centered on the galaxy. This physical volume is selected to cover the radial extent of the multi-armed spiral pattern of NGC 6946 which is well approximated by an 8 kpc galactocentric radius. The scale

Table 5.1: Model parameters.

	Description	Standard	Best-fit	Sample range
p_0 [°]	pitch angle of field at mid-plane	28^*	28	
p_∞ [°]	pitch angle of field at infinity	90	n.a.	
z_1 [kpc]	model reference height	0.5	5	0.5 – 14
H_p [kpc]	reference height for pitch angle	5	∞	$2, 4, 8, 16, \infty$
L_B [kpc]	exp. scale length of ref. field	3	3	0.5 – 5
$n_{\rm e,disk}$ [$\rm cm^{-3}$]	thermal electron density in disk	0.03^*	0.03	0.03, 0.3
$n_{\rm e,halo}$ [$\rm cm^{-3}$]	thermal electron density in halo	0.003^*	0.03	0, 0.003, 0.03, 0.3
L_d [kpc]	scale height of thermal disk	0.5^*	0.5	0.5
L_h [kpc]	scale height of thermal halo	5	5	5, 7.5
B_1 [μG]	peak value of the ref. field	0 – 50	37^{+5}_{-6}	0 – 100
$\langle B \rangle$ [μG]	average regular magnetic field		12 ± 2	

Notes: $^{(*)}$ Equal to literature values, see text.

height of the non-thermal emission at λ20 cm is $\sim$ 4 kpc (Walsh et al. 2002), which is well contained in our model box. As it is the non-thermal emission that we use to fit the models, 8 kpc is a very reasonable vertical extent.

5.4 Method

We partition the $p_{\rm obs}$ maps into four radial rings, centered on NGC 6946's center, with ring boundaries every 1.6 kpc from 1.6−8.0 kpc. The 1.6 kpc incremental distance corresponds to four times the beam size. Every such ring is subdivided into 18 azimuthal sectors, each with an opening angle of 20°, see Fig. 5.1. The number of resolution elements per bin therefore ranges from 7 – 21 elements from the inner ring to the outer ring. This results in a total of 72 bins per map and provides a good sampling of the depolarization features. For each of the bins, the mean of $p_{\rm obs}$ is computed with the standard deviation of $p_{\rm obs}$ taken as the error.

To obtain a model of the degree of polarization ($p_{\rm mod}$), we take an initial 6D parameter space characterized by z_1, $H_{\rm p}, L_{\rm B}$, $n_{\rm e}$ in the disk and halo, and B_1. Next, we define a standard model by setting each of these parameters to a physically motivated constant with the exception of B_1 which is the only independent parameter. The standard model parameters are displayed in Table 5.1. The value of z_1 corresponds to the value of L_d, that of $H_{\rm p}$ corresponds to L_h, and the value of $L_{\rm B}$ is selected because it roughly reproduces the observed, approximately constant, profile of magnetic field strength with galactic radius along the disk as shown in Beck (2007, Fig. 5). The thermal electron density and path length through the disk and halo are not known and these values are roughly based on those found for the disk in the models of Ehle & Beck (1993) and Beck (2007) which assumed Milky Way parameters. The thermal electron density in the disk is consistent with the thermal density of $n_{\mathrm{e,disk}} = 0.05\ \mathrm{cm}^{-3}$ typically assumed for galactic disks (Ferrière 2001).

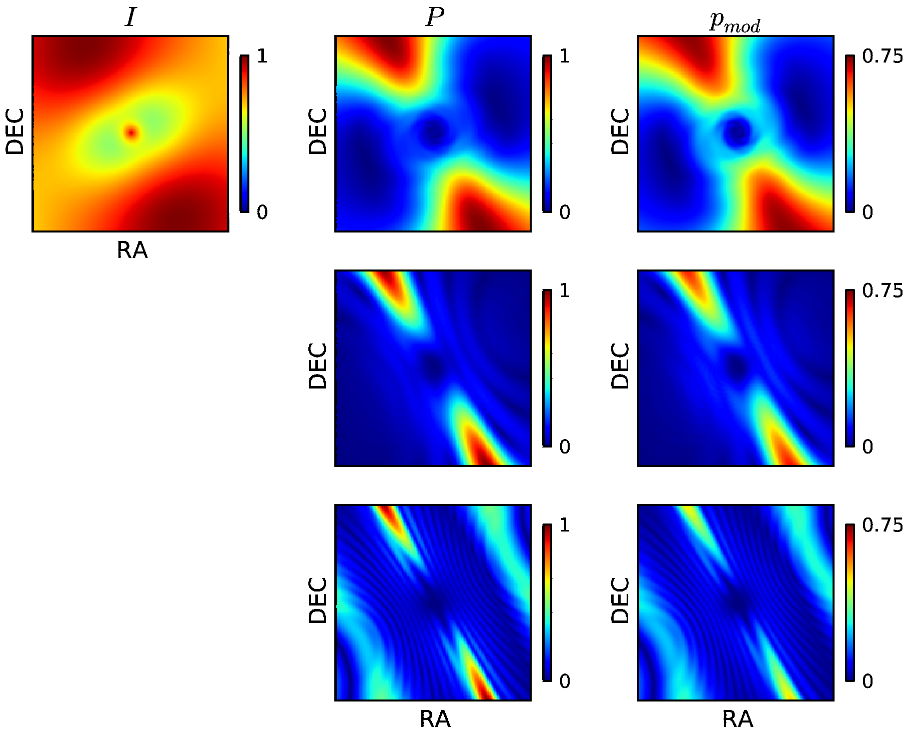

Figure 5.4: Proceeding from the left to right: model outputs of total intensity (I) which has been normalized, polarized intensity (P) which has also been normalized, and degree of polarization (p_{mod}). I, P, and p_{mod} are presented for the best-fit model (see Section 5.5) with P and p_{mod} shown at 6 cm (top), 13 cm (middle), and 23 cm (bottom). The receding side of the galaxy is towards the West.

The standard model is shown in Fig. 5.2 with the full 3D field shown (top left). In the disk, the ASS field is even and points inward (top right), following the direction of the observed optical spiral arms. In the halo, the magnetic field is also even and points outward from the mid-plane, exhibiting a quadrupolar morphology (bottom two panels). These combined ingredients yield p_{mod} via the Stokes parameters which are then compared to p_{obs} to find the best-fit magnetic field strength B_1.

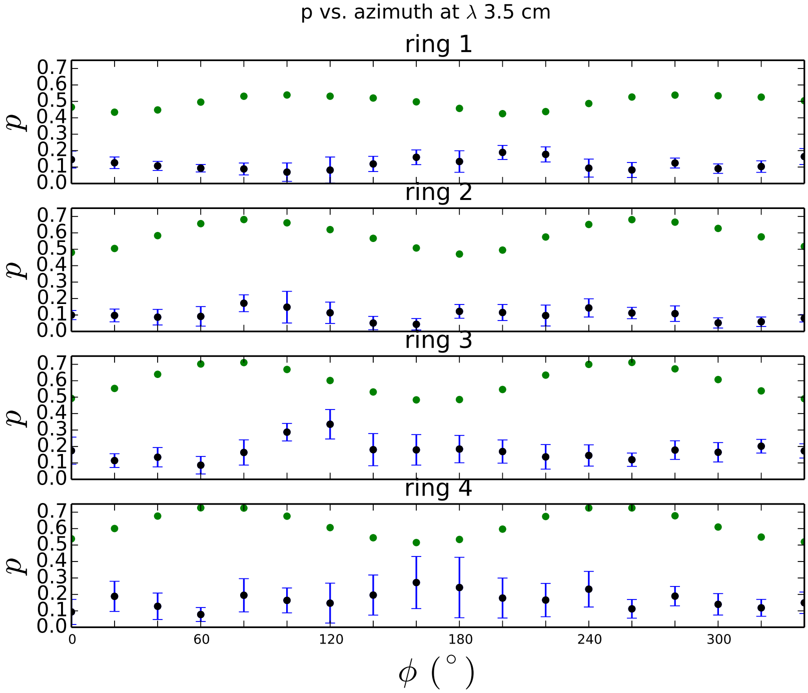

Figure 5.5: The azimuthal variation of the degree of polarization (p) is presented at the lowest observing wavelength of 3 cm in rings 1-4 proceeding from top to bottom. The mean value of the observed p are shown in solid blue points at every azimuthal bin in a ring with associated error bars given by the standard deviation of p in a given bin. The modeled p values without scaling by the factor A (see Section 5.5) are indicated with solid green points. The azimuthal angle (ϕ) is measured counter-clockwise from the receding side of the major axis.

5.4.1 Goodness of fit

A reduced chi-square statistic is computed using all the data bins simultaneously. The reduced chi-square statistic is given by

$$\chi^2_{\text{red}} = \frac{1}{N} \sum_{\text{bins}} \frac{(p_{\text{obs}} - A * p_{\text{mod}})^2}{\sigma_p^2}, \tag{5.11}$$

with $A = (p_{\text{obs},\,\lambda 3.5\text{cm}}/p_{\text{mod},\,\lambda 3.5\text{cm}})$ a parameter estimating the contribution of wavelength-independent depolarization, see Section 5.5. σ_p is the standard deviation of the measured p values per bin, the sum is taken over all bins, and N is the number of degrees of freedom given by (*# observing wavelengths*) × (*# bins*) − (*# independent parameters*). With the regular field strength as the only independent parameter, the number of degrees of freedom is $N = 2951$.

We test the robustness of our best-fit B_1 value and estimate an uncertainty in this parameter using a bootstrap technique introduced in Chap. 4. Keeping all best-fit model parameters fixed, except for B_1, we again vary B_1 from $0-50\,\mu$G. However, at each value of B_1, we now discard 30% of all azimuthal p bins at random in each ring for all four rings for a fixed observing frequency and compute $\chi^2_{\rm red}$ for 50 independent trial runs. For our large number of degrees of freedom, the chi-square distribution approaches a normal distribution. Subsequently, the mean and standard deviation of $\chi^2_{\rm red}$ corresponding to the best-fit B_1 field strength, over 50 independent trials, is used to establish the range of all other admissible B_1 values and thus the error in the average best-fit regular magnetic field strength. The B_1 values which define the admissible range satisfy the condition that their mean $\chi^2_{\rm red}$ values fall within 1σ of the best-fit $\chi^2_{\rm red}$ mean value.

5.5 Results

The best-fit model has a 3D regular magnetic field configuration, with a reduced chi-square statistic of $\chi^2_{\rm red} = 8.5$, and its parametrization is given in Table 5.1. This model yields a mean regular magnetic field value of $12 \pm 2\,\mu$G in close agreement with estimates given in Beck (2007). This best-fit model was produced assuming a synchrotron spectral index of -0.7, characteristic of the optical spiral arms, which gives better results than the spectral index of -1.0 representative of the interarm regions (Section 5.2). The best-fit magnetic field configuration is shown in Fig. 5.3 and exhibits a pronounced vertical component above and below the central region which is in agreement with magnetic field configurations found in several edge-on spiral galaxies such as NGC 253 in Heesen et al. (2009, Fig. 16) and NGC 5775 in Soida et al. (2011, Fig. 12).

The model outputs of I and P, and p are shown in Fig. 5.4. As expected from the dependence of both I and P on the magnetic field component perpendicular to the line of sight ($B_\perp$), their pairs of maxima and minima occur at the locations of the minor and major axes respectively, though are slightly offset as a result of projection (Braun et al. 2010). However, the modeled Stokes I in Fig. 5.4 shows an increase in intensity in the direction of the minor axis which is not observed (Beck 2007, Fig. 1). We tried an alternative set of models in the range $1 \leq L_B < 3$ kpc with varying values of z_1 which did reproduce the observed radially decreasing intensity. These models, nonetheless, resulted in unbounded values for the regular magnetic field, suggesting that the best-fit magnetic field was higher than the (observationally motivated) field strengths that were probed. As a consequence of the increasing amount of depolarization at longer wavelengths, the value of the $p_{\rm mod}$ maps decrease with increasing wavelength.

Comparing the $p_{\rm mod}$ maps in Fig. 5.4 with the $p_{\rm obs}$ maps in Fig. 5.1 reveals differences in the modeled and observed depolarization patterns. Figure 5.5 shows a comparison between model and observations at $\lambda\,3.5$ cm for all bins. Clearly, the model greatly overestimates the polarization degree. This most likely results from the model not accounting for the turbulent component of the magnetic field, which depolarizes. As a first-order approach to correcting this, we include wavelength-independent depolarization only. We assume that all depolarization is wavelength-independent at $\lambda\,3.5$ cm (i.e. no significant

Faraday rotation at $\lambda\,3.5$ cm) and scale the modeled p at $\lambda\,3.5$ cm to the observed ones. This is done by the factor A in Eq. (5.11).

The best-fit model including wavelength-independent depolarization reproduces the observed azimuthal variation of p in the inner two rings but deviates in the outer two rings as shown in Fig. 5.6 for the innermost and outermost part of the galaxy. As expected on the basis of the above scaling by the factor A, p_{mod} coincides exactly with p_{obs} at the lowest observing wavelength of 3.5 cm in all four figures. In the inner galaxy, p_{mod} generally overestimates p_{obs}, while in the outer galaxy, p_{obs} is mostly underestimated. Figure 5.7 shows the wavelength dependence of the depolarization for each bin in the innermost and outermost part of the galaxy. The general decrease with wavelength is reproduced well by the models, although the overestimation of p_{obs} in the inner galaxy is visible in this figure too. Also, the model shows increases of p with increasing wavelength in the outer galaxy for some azimuths, which are not observed. We discuss the discrepancy between observations and model in Section 5.6.

5.5.1 Sensitivity to input parameters

In order to efficiently sample the previously described 6D parameter space, we have made excursions from our standard parameter model, separately for each parameter, while varying B_1 from $0 - 50\,\mu$G. These sample ranges are presented in Table 5.1.

The B_1 value is a robust estimator of the best-fit regular field strength as it does not fluctuate too much when portions of the data are discarded at random (see Section 5.4.1). As Fig. 5.8 shows, the variance decreases for lower chi-square values at larger magnetic field values and the minimum chi-square plateau arising from 50 independent trials lies within the best-fit range determined in Section 5.5.

Our best-fit model is not very sensitive to the exact value of H_p as the sampled range of H_p in Table 5.1 yields similar χ^2_{red} values of about 9. This trend was taken to indicate that the minimum χ^2_{red} value would be achieved when the pitch angle would simply be fixed at its mid-plane value everywhere ($H_p = \infty$). This is not an unreasonable choice as p_0 is observed to remain fairly constant with galactic radius of up to 12 kpc in the disk of NGC 6946 (Ehle & Beck 1993). It is clear from the models tested that $n_{\mathrm{e,disk}} = 0.03\ \mathrm{cm}^{-3}$ is a good value to use and that the presence of a thermal halo is required with a density equal to that of the disk. This would mean that the thermal electron density in the halo of NGC 6946 is higher than that of the Milky Way, which is estimated as $n_{\mathrm{e}} = 0.003\ \mathrm{cm}^{-3}$. The output values are most dependent on variation in the value of z_1. Figure 5.9 shows the dependence of χ^2_{red} on the variation in z_1 and B_1. For an initial coarse sampling of B_1 in steps of $4\,\mu$G, Fig. 5.9 shows that $z_1 = 5$ kpc gives the best fit ($\chi^2_{\mathrm{red}} = 9.2$) for $B_1 = 36\,\mu$G consistent with the value $B_1 = 37^{+5}_{-6}\,\mu$G found with finer sampling of B_1 for fixed z_1.

5.6 Discussion

Our model explains part of the observations, but also contains features not in agreement with our data or earlier literature. We will discuss both similarities and differences accom-

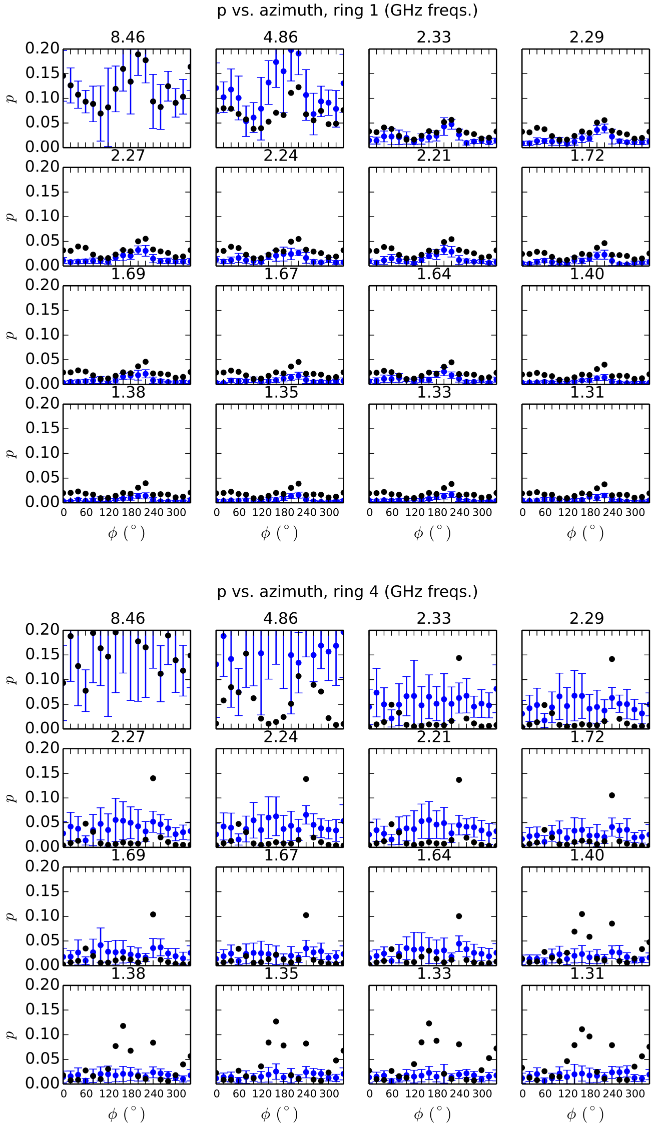

Figure 5.6: The azimuthal variation of the degree of polarization (p) is presented at the two lowest observing wavelengths of 3.5 and 6 cm (first two plots of the top row in both sub-figures) and subsequently at every third wavelength from 13 cm - 23 cm. The mean value of the observed p are shown in solid blue points at every azimuthal bin in ring 1 (innermost ring) in the top sub-figure and in ring 4 (outermost ring) in the bottom sub-figure with associated error bars given by the standard deviation of p in a given bin. The modeled p values are indicated with solid dark points.

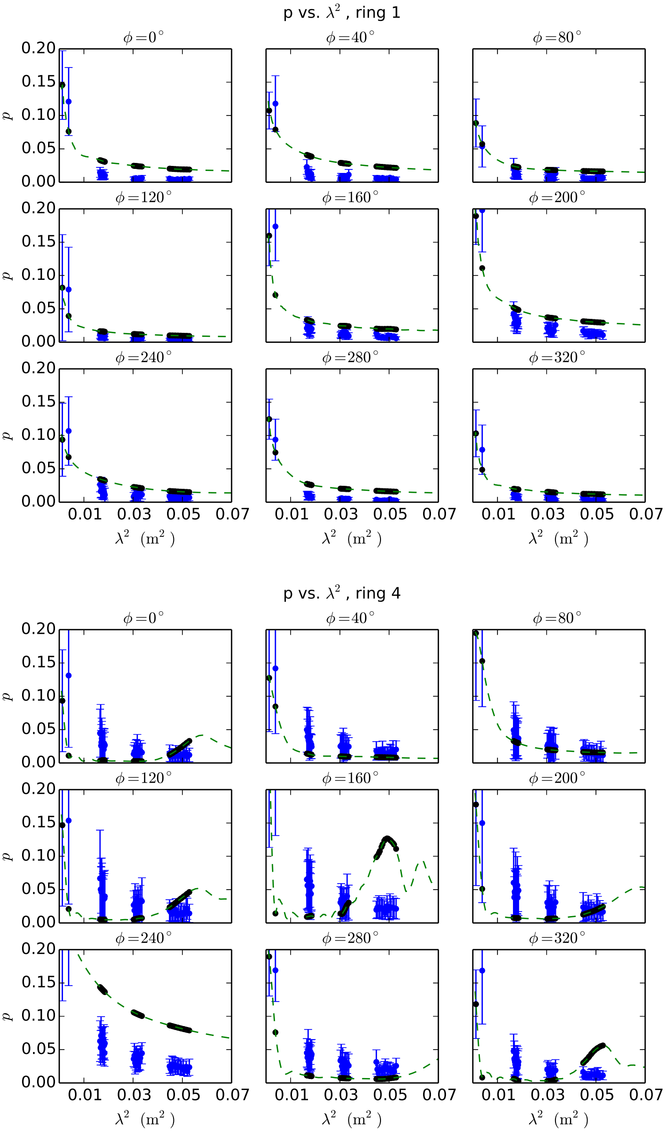

Figure 5.7: The variation of p with the square of the observing wavelength λ^2 (m^2) is presented for the 42 available wavelengths between 3.5 cm to 23 cm at every second of the 18 azimuthal bins (0° – 320° in steps of 40°) comprising ring 1 (innermost ring) in the top sub-figure and ring 4 (outermost ring) in the bottom sub-figure. The mean value of the observed p are shown in solid blue points at every second azimuthal bin in rings 1 and 4 with associated error bars given by the standard deviation of p in a given bin. The modeled p values are indicated with solid dark points. The dashed green line simulates a continuous wavelength coverage spanning 3 cm - 26.5 cm.

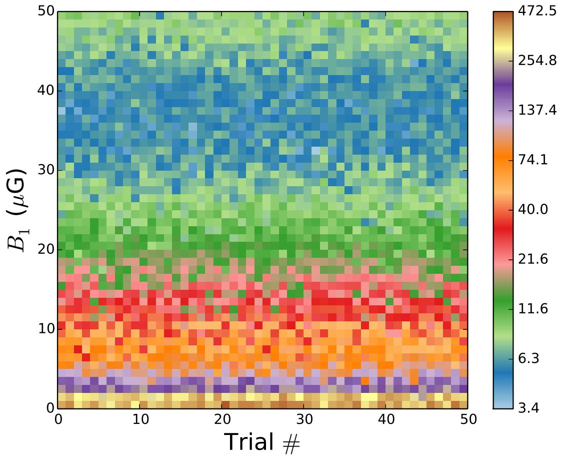

Figure 5.8: Map of reduced chi-square values obtained using the bootstrap technique (see Section 5.4.1) with 50 independent trial runs for each B_1 value.

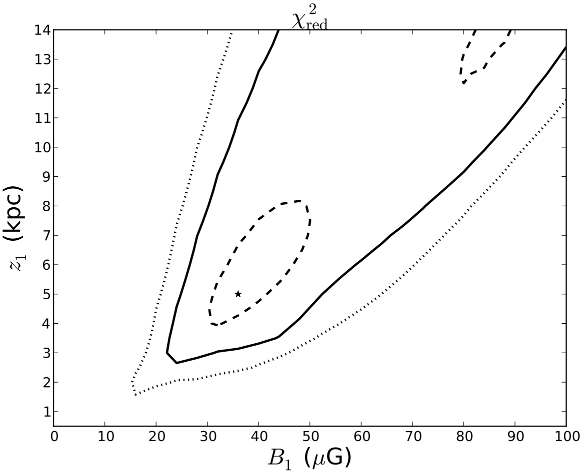

Figure 5.9: Contours of reduced chi-square values for regular magnetic field strength B_1 and height above the mid-plane z_1 for the entire modeled galaxy. The best-fit z_1 and B_1 combination is denoted by ★. The dashed, solid, and dotted contours represent $10, 50,$ and 100 percent increases in the minimum χ^2_{red} value, respectively.

panied by a possible explanation or way to continue. Our model agrees with a number of galaxy observations (Urbanik et al. 1997; Heesen et al. 2009; Soida et al. 2011; Mora & Krause 2013) and models (Braun et al. 2010). Its features agree with helical magnetic field models of M 83 and NGC 6946 by Urbanik et al. (1997), who conclude that an extended gaseous and magnetic halo is required, and that the azimuthal field could not be much stronger than the poloidal one. Our best-fit model shows similarities to some of the models described in Braun et al. (2010), in particular the axisymmetric disk field, X-shaped halo fields and a comparable magnetic field scale height.

Our model does not describe wavelength-dependent depolarization due to turbulence. However, no wavelength-dependent discrepancy is seen in p_{obs} in Fig. 5.7 which suggests that this effect can be neglected. The overestimation of p_{mod} in the inner galaxy and underestimation of p_{mod} in the outer galaxy indicates that p_{mod} decreases with radius faster than p_{obs}. This could be the result if the magnetic field strength decreases faster as a function of radius in reality than in the model or if there is more turbulence in the inner galaxy than in the outer galaxy which would cause more depolarization in the inner galaxy.

The abrupt rise in p_{mod} at the longest observing wavelengths in the bottom sub-figure of Fig. 5.7 for particular values of the azimuth corresponds to the locations of the two 'secondary maxima' fringe regions (diagonally oriented and parallel to the two expected maxima) at $\lambda\,23$ cm in Fig. 5.4. These fringe regions arise from the interplay between Faraday depth and synchrotron intensity in a multilayer magneto-ionic medium. For the case of a medium consisting of two uniform layers, Chadderton (2011) have shown that complete depolarization will not occur (at any wavelength) if both the following two conditions are satisfied: the layer farthest from the observer must have a much higher Faraday depth than the layer closest to the observer and the layer closest to the observer must constitute some fraction of the total intensity. Although our model does not have a constant magnetic field as in the uniform-layer model, lines of sight that probe the magneto-ionic volume in the outer galaxy may satisfy such conditions at certain azimuths. Since these fringes disappear if the galaxy is taken to be exactly face-on ($l = 0°$), their apparent parallel alignment with the expected two maxima is a result of projection. Alternatively, the absence of these fringe features in p_{obs} may indicate their effective erasure by depolarization from isotropic turbulent magnetic fields or that our X-shape regular magnetic field model requires vertical fields originating at larger radii.

5.7 Summary and conclusions

We constructed a simple analytical model of a 3D regular magnetic field in spiral galaxy NGC 6946. This field model has a vertical field component as observed in a number of edge-on spiral galaxies, and is modeled divergence-free Ferrière & Terral (2014). This magnetic field model, combined with thermal and cosmic ray electron distributions, predicts a degree of polarization at radio wavelengths comparable with multi-frequency radiopolarimetric observations of NGC 6946 Williams & Heald (2015).

The model reproduces the observed azimuthal variation of polarization degree, especially in the inner galaxy. The best-fit average magnetic field strength is $12 \pm 2\,\mu$G, consistent with earlier estimates, and extends out to a vertical height of 5 kpc from the plane. However, the best-fit model shows an unexplained increase in Stokes I away from the plane, which can only be mitigated with unphysically high magnetic field strengths. Also, at some azimuths, unobserved increases in polarization degree occur in the model. In summary, our magnetic field model including an out-of-plane, X-shaped magnetic field component can reproduce some of the main features of the radiopolarimetric observations, but needs additional complexity to fit the data well.

5.8 Future work

The first priority is finding the reason why the current model does not fit the data well enough. In particular, the model predicts an increase in Stokes I at larger distances from the plane and 'spokes' of high polarization at certain azimuths. Also, modeled RMs are higher than those observed by Beck (2007), which should be improved. Whether our proposed explanation for the absence of these features in the observations is valid and whether a closer agreement with the observations through parameter adaptation may be attained, remains to be demonstrated.

The modeling mechanism itself can be improved in a number of ways. Firstly, the error analysis could be performed in a more rigorous manner by determining the error in B_1 based on small variations in all other model parameters. Second, a more refined approach would be to dispense with rings and sectors altogether and compare model with data in each pixel individually. We could then follow smaller-scale trends in the data better with the model (e.g. distinguishing between spiral arms and interarm regions).

The current model for magnetic field and other galactic components is very simplified. The current magnetic field model could be refined by specifically adding a turbulent component of the field, based on appropriate estimates. Estimates of the total turbulent field such as in Tabatabaei et al. (2013) would be useful in this respect. Also, a low-amplitude quadrisymmetric mode ($m = 2$) to the axisymmetric mode ($m = 0$) in the disk as advocated by Beck et al. (1996); Rohde et al. (1999); Beck (2007) might improve correspondence of the model to the observations. Other possible model refinements would include a variable spectral index (e.g. in spiral arms and interarm regions), based on observational data, and/or a variable cosmic ray electron distribution.

Acknowledgements

CS and MH acknowledge the support of research program 639.042.915, which is partly financed by the Netherlands Organization for Scientific Research (NWO). CS and MH are thankful to Katia Ferrière for enlightening comments on galactic magnetic fields. The simulations were performed on the Coma Cluster at Radboud University, Nijmegen, The Netherlands.

Bibliography

Beck, R. 2007, A&A, 470, 539

Beck, R., Brandenburg, A., Moss, D., Shukurov, A., & Sokoloff, D. 1996, ARA&A, 34, 155

Beck, R. & Wielebinski, R. 2013, Magnetic Fields in Galaxies, ed. T. D. Oswalt & G. Gilmore, 641

Berkhuijsen, E. M., Horellou, C., Krause, M., et al. 1997, A&A, 318, 700

Boomsma, R., Oosterloo, T. A., Fraternali, F., van der Hulst, J. M., & Sancisi, R. 2008, A&A, 490, 555

Boulares, A. & Cox, D. P. 1990, ApJ, 365, 544

Brandenburg, A., Donner, K. J., Moss, D., et al. 1993, A&A, 271, 36

Braun, R., Heald, G., & Beck, R. 2010, A&A, 514, A42

Braun, R., Oosterloo, T. A., Morganti, R., Klein, U., & Beck, R. 2007, A&A, 461, 455

Chadderton, R. 2011, MSc Thesis Newcastle University

Dahlem, M., Petr, M. G., Lehnert, M. D., Heckman, T. M., & Ehle, M. 1997, A&A, 320, 731

Dalla Vecchia, C. & Schaye, J. 2008, MNRAS, 387, 1431

Dalla Vecchia, C. & Schaye, J. 2012, MNRAS, 426, 140

Ehle, M. & Beck, R. 1993, A&A, 273, 45

Ferguson, A., Wyse, R., & Gallagher, J. 1999, in Astronomical Society of the Pacific Conference Series, Vol. 170, The Low Surface Brightness Universe, ed. J. I. Davies, C. Impey, & S. Phillips, 196

Ferrière, K. & Terral, P. 2014, A&A, 561, A100

Ferrière, K. M. 2001, Reviews of Modern Physics, 73, 1031

Fletcher, A., Beck, R., Shukurov, A., Berkhuijsen, E. M., & Horellou, C. 2011, MNRAS, 412, 2396

Gressel, O., Elstner, D., & Ziegler, U. 2013, A&A, 560, A93

Hanasz, M., Otmianowska-Mazur, K., Kowal, G., & Lesch, H. 2009a, A&A, 498, 335

Hanasz, M., Wóltański, D., & Kowalik, K. 2009b, ApJ, 706, L155

Hanasz, M., Woltanski, D., & Kowalik, K. 2013, in IAU Symposium, Vol. 294, IAU Symposium, ed. A. G. Kosovichev, E. de Gouveia Dal Pino, & Y. Yan, 225–236

Haverkorn, M. 2014, ArXiv e-prints

Haverkorn, M. & Spangler, S. R. 2013, Plasma Diagnostics of the Interstellar Medium with Radio Astronomy, ed. A. Balogh, A. Bykov, P. Cargill, R. Dendy, T. Dudok de Wit, & J. Raymond, 407
Heald, G. 2014, in prep
Heald, G., Braun, R., & Edmonds, R. 2009, A&A, 503, 409
Heesen, V., Brinks, E., Leroy, A. K., et al. 2014, AJ, 147, 103
Heesen, V., Krause, M., Beck, R., & Dettmar, R.-J. 2009, A&A, 506, 1123
Hennebelle, P. & Falgarone, E. 2012, A&A Rev., 20, 55
Jansson, R. & Farrar, G. R. 2012a, ApJ, 757, 14
Jansson, R. & Farrar, G. R. 2012b, ApJ, 761, L11
Kennicutt, Jr., R. C. 1981, AJ, 86, 1847
Kennicutt, Jr., R. C., Armus, L., Bendo, G., et al. 2003, PASP, 115, 928
Krause, M. 2009, in Revista Mexicana de Astronomia y Astrofisica Conference Series, Vol. 36, Revista Mexicana de Astronomia y Astrofisica Conference Series, 25–29
Krause, M. 2014, ArXiv e-prints
Kulpa-Dybeł, K., Otmianowska-Mazur, K., Kulesza-Żydzik, B., et al. 2011, ApJ, 733, L18
Mora, S. C. & Krause, M. 2013, A&A, 560, A42
Moss, D., Sokoloff, D., Beck, R., & Krause, M. 2010, A&A, 512, A61
Orlando, S., Bocchino, F., Reale, F., Peres, G., & Pagano, P. 2008, ApJ, 678, 274
Parker, E. N. 1971, ApJ, 163, 255
Parker, E. N. 1979, Cosmical magnetic fields: Their origin and their activity
Rohde, R., Beck, R., & Elstner, D. 1999, A&A, 350, 423
Shneider, C., Haverkorn, M., Fletcher, A., & Shukurov, A. 2014a, A&A, 568, A83
Shneider, C., Haverkorn, M., Fletcher, A., & Shukurov, A. 2014b, A&A, 567, A82
Soida, M., Krause, M., Dettmar, R.-J., & Urbanik, M. 2011, A&A, 531, A127
Sokoloff, D. D., Bykov, A. A., Shukurov, A., et al. 1998, MNRAS, 299, 189
Sokoloff, D. D., Bykov, A. A., Shukurov, A., et al. 1999, MNRAS, 303, 207
Steenbeck, M. & Krause, F. 1966, Zeitschrift Naturforschung Teil A, 21, 1285
Strong, A. W., Moskalenko, I. V., & Ptuskin, V. S. 2007, Annual Review of Nuclear and Particle Science, 57, 285
Tabatabaei, F. S., Schinnerer, E., Murphy, E. J., et al. 2013, A&A, 552, A19
Tüllmann, R., Dettmar, R.-J., Soida, M., Urbanik, M., & Rossa, J. 2000, A&A, 364, L36
Urbanik, M., Elstner, D., & Beck, R. 1997, A&A, 326, 465
Vainshtein, S. I. & Ruzmaikin, A. A. 1971, AZh, 48, 902
Walsh, W., Beck, R., Thuma, G., et al. 2002, A&A, 388, 7
Williams, A. & Heald, G. 2015, in prep
Yan, H. 2015, in Astrophysics and Space Science Library, Vol. 407, Astrophysics and Space Science Library, ed. A. Lazarian, E. M. de Gouveia Dal Pino, & C. Melioli, 253